18385

Surface Passivation of Nanoporous TiO₂ via Atomic Layer Deposition of ZrO₂ for Solid-State Dye-Sensitized Solar Cell Applications

Tina C. Li,[†] Márcio S. Góes,[‡,§] Francisco Fabregat-Santiago,*,[‡] Juan Bisquert,[‡] Paulo R. Bueno,[§] Chaiya Prasittichai,[†] Joseph T. Hupp,*,[†] and Tobin J. Marks[†]

Department of Chemistry and the Argonne−Northwestern Solar Energy Research Center, Northwestern University, Evanston, Illinois 60208-3113, Photovoltaic and Optoelectronic Devices Group, Departament de Física, Universitat Jaume I, 12071 Castelló, Spain, and Departamento de Físico-Química, Instituto de Química de Araraquara, Universidade Estadual Paulista, R. Prof. Francisco Degni s/n, 14800-900 Araraquara SP, Brazil

Received: July 12, 2009; Revised Manuscript Received: August 22, 2009

We report here the utilization of atomic layer deposition to passivate surface trap states in mesoporous TiO₂ nanoparticles for solid-state dye-sensitized solar cells based on 2,2′,7,7′-tetrakis(*N,N*-di-*p*-methoxyphenylamine)-9,9′-spirobifluorene (spiro-OMeTAD). By depositing ZrO₂ films with angstrom-level precision, coating the mesoporous TiO₂ produces over a two-fold enhancement in short-circuit current density, as compared to a control device. Impedance spectroscopy measurements provide evidence that the ZrO₂ coating reduces recombination losses at the TiO₂/spiro-OMeTAD interface and passivates localized surface states. Low-frequency negative capacitances, frequently observed in nanocomposite solar cells, have been associated with the surface-state mediated charge transfer from TiO₂ to the spiro-OMeTAD.

Introduction

Dye-sensitized solar cells (DSCs) based on mesoporous titania and liquid electrolytes have been presented as a promising renewable energy source, achieving power conversion efficiencies greater than 11%.[1] However, leakage of the commonly used I⁻/I₃⁻ redox electrolyte, with consequent compromise of long-term cell stability, has prompted efforts to find an efficient hole conductor for all solid-state DSCs (Figure 1). While the performance of solid-state DSCs (ssDSCs) is usually much lower than that with liquid electrolytes, the efficiencies of devices based on the molecular organic semiconductor spiro-OMeTAD have recently advanced.[2] Nevertheless, device performance is still constrained by competing transport and recombination dynamics, and electron diffusion lengths are limited to a few micrometers.[3]

Like their liquid counterparts, ssDSCs generally rely on a network of sintered nanocrystalline TiO₂ particles, sensitized with a monolayer of a ruthenium-containing dye.[4−6] Upon illumination, the sensitizer is excited by absorption of a photon and injects an electron into the conduction band of the semiconductor. Electron transport through the titanium oxide framework can be described by a trapping/detrapping model, where an electron moves from trap-to-trap until collection at the cell's transparent conducting oxide anode. The hole conductor transports the hole remaining in the oxidized dye to the cathode via a hopping mechanism.[7]

The collection efficiency of injected electrons in DSCs is less than unity on account of charge recombination processes. For ssDSCs, the principle charge losses come from "interception", i.e., deleterious recombination of the electrons in the TiO₂ and the holes in the spiro-OMeTAD, due to the close contact
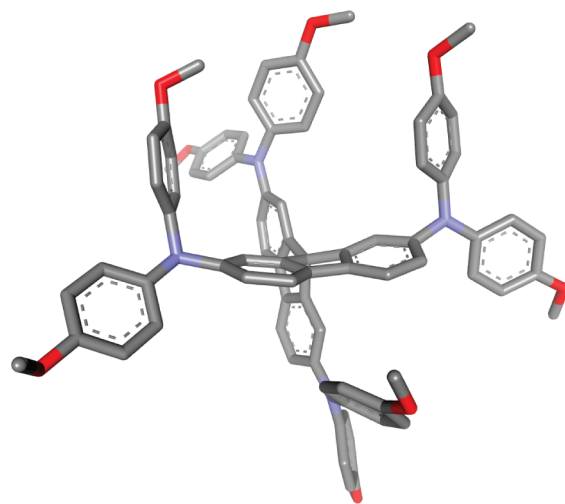

Figure 1. MM2 energy minimization of the solid-state hole conductor, spiro-OMeTAD, used to replace I⁻/I₃⁻ (hydrogens omitted for clarity; carbons are gray, nitrogens are blue, and oxygens are red).

between the two phases.[5,8] In comparison to liquid-junction DSCs, this effect is even more acute by lower charge screening, due to the lower ion mobility in the solid-state phase.

Strategies to reduce interfacial interception have involved decreasing the TiO₂ electrode thickness below 3 μm, adding ionic salts to the spiro-OMeTAD solution,[9] replacing the traditional "N719" ruthenium polypyridyl sensitizer with the hydrophobic analogue "Z907",[10] and inserting insulating layers between the TiO₂ and hole transport medium to prevent back reaction of the electrons.[11] Previously, dip-coating methods were employed to coat tunneling layers onto the nanoporous TiO₂ electrode[12−14] (i.e., Al₂O₃, MgO, SiO₂); however, control of the film growth through this technique is problematic, and comparatively thick films are required to ensure complete coverage. Here, we address the importance of the inorganic/organic

* To whom correspondence should be addressed. E-mail: fabresan@fca.uji.es and j-hupp@northwestern.edu.
† Northwestern University.
‡ Universitat Jaume I.
§ Universidade Estadual Paulista.

interface in the solid-state DSC system, where recombination plays a major role. By using atomic layer deposition (ALD),[15−17] we initiate slow and conformal growth of ZrO_2 onto the TiO_2 nanoparticles to passivate surface trap states, leading to significant enhancements in short-circuit current densities and overall power conversion efficiencies.

Impedance spectroscopy (IS) is a powerful technique to investigate the kinetic processes in DSCs.[18−21] Under the appropriate conditions, several processes can be readily distinguished according to the spectral shapes of the impedance response as a function of frequency, and recently, the major features of IS in spiro-OMeTAD based DSCs were explicated.[22] Such methods are applied in this paper to identify the effects on ssDSC performance of depositing ZrO_2 coatings of varying thickness on the TiO_2 nanoparticles with attention focused on the various interception processes. Importantly, for progressively thicker ZrO_2 coating levels, we find a reduction of the inductive behavior at low frequencies; inductive behavior is known to be a performance-limiting factor in other types of solar cells[23] as well as in some organic light-emitting diodes.[24] For the first time, the experimental evidence clearly indicates that the spatial origin of the inductive component of nanostructured solar cell impedance is at the metal oxide/hole conductor interface.

Experimental Methods

All solvents were purchased from Sigma-Aldrich as anhydrous grade or higher. Acetonitrile was further purified according to published methods.[25] Chlorobenzene was dried over phosphorus pentoxide and distilled under dry nitrogen. The hole conductor spiro-OMeTAD was synthesized and purified as published[26] and solid-state devices using spiro-OMeTAD were prepared as previously described.[27] Patterned fluorine-doped tin oxide (FTO) electrodes on glass (Hartford Glass, TEC 15) were used with a dense, compact blocking layer of TiO_2 (the back layer), deposited via spray pyrolysis,[28] yielding 120 nm thick anatase films. TiO_2 paste (Dyesol, DSL-90-T) diluted with terpineol was screen-printed directly onto this underlayer, and sintered at 500 °C for 30 min. The resulting 1.8 μm mesoporous films were treated with UV-ozone for 10 min and immediately transferred to the ALD chamber (Savannah 100 ALD instrument, Cambridge Nanotech, Inc.) for ZrO_2 growth at 200 °C. Alternating pulses of the precursors $Zr(NMe_2)_4$ and H_2O were used, with reaction exposure times of 1 and 5 s, respectively, achieving a growth rate of 1.1 Å/cycle, as determined by ellipsometry on flat platforms. Prior to dye loading, the electrodes were again treated with UV-ozone and immersed in a 0.3 mM solution of *cis*-bis(isothiocyanato)bis(2,2′-bipyridyl-4,4′-dicarboxylato)ruthenium(II) bis(tetrabutylammonium) (Dyesol, N719) in CH_3CN:*tert*-butyl alcohol (50:50 vol %) for 10 h.

A 0.17 M solution of spiro-OMeTAD was prepared in chlorobenzene, adding 0.3 mM $[N(p\text{-}C_6H_4Br)_3](SbCl_6)$, 20.4 mM $Li[(CF_3SO_3)_2N]$, and 0.13 M *tert*-butylpyridine dissolved in acetonitrile. These additives serve to control the doping level of the spiro-OMeTAD and also to enhance conductivity as well as overall cell performance.[29] The hole conductor solution was drop-cast onto the dye-sensitized TiO_2 films and allowed to infiltrate the pores before spin-casting at 1800 and 260 rpm/s acceleration for 40 s. Excess solution was carefully wiped with toluene and the films were dried overnight in a vacuum oven at 55 °C. A 50 nm gold electrode was then thermally evaporated under high vacuum (10^{-6} Torr) at <0.2 Å/s to complete the cell. Characteristic parameters of the ssDSCs were obtained by illuminating the samples with an AM 1.5 solar simulator (1000 W, class A, from Newport, 91192-A) at 100 mW cm^{-2}. The
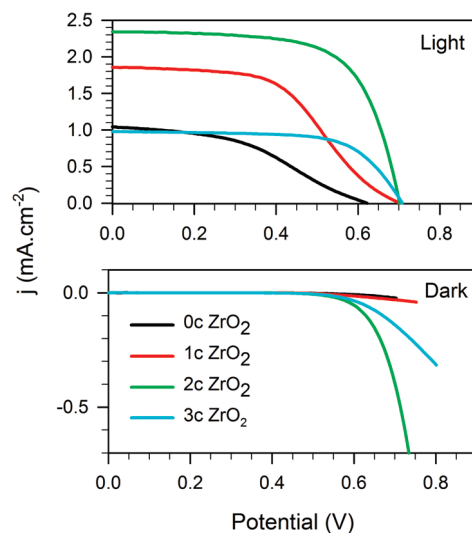

Figure 2. Current−voltage characteristics of solid-state DSCs having 0 to 3 ALD deposition cycles of ZrO_2 coating on the TiO_2. Measurements were taken under 100 mW/cm^2 illumination (top panel) and in the dark (bottom panel).

current−voltage (j−V) data were registered with a PGSTAT-30 (Autolab) that was also used for IS measurements. Impedance spectra were taken at bias potentials ranging between 0 and −0.85 V both in the dark and under illumination. The amplitude of the ac signal used was 20 mV, and the frequency ranged between 1 MHz and 10 mHz.

Open-circuit voltage decay measurements were performed with a fluorimeter as an illuminator (Jobin-Yvon fluorescence spectrometer) and a CH Instruments 1202 potentiostat. Data obtained with this technique for solid-state DSC will be compared with those of liquid-electrolyte I^-/I_3^- based DSCs fabricated as reported previously.[30] Briefly, the liquid-junction cells were fabricated with 4 μm thick TiO_2 electrodes, sensitized with N719. The electrolyte consisted of 0.60 M 1-butyl-3-methylimidazolium iodide, 0.03 M I_2, 0.10 M guanidinium thiocyanate, and 0.50 M 4-*tert*-butylpyridine in acetonitrile:valeronitrile (85:15). The TiO_2 films were conformally coated with ZrO_2 via ALD following the procedure described above. Short-circuit current densities for cells featuring 0, 1, 2, and 3 cycles of ZrO_2 coating were 6.2, 5.4, 4.4, and 3.1 mA/cm^2, respectively.

Results and Discussion

Atomic layer deposition was chosen to deposit barrier layers, since it ensures well-defined, conformal growth. By inserting a physical barrier at the dye interface, direct contact between the titanium oxide and spiro-OMeTAD is prevented, slowing the back reaction of electrons to the hole transport medium. However, ZrO_2 ALD is unable to provide complete coverage of the electrodes with a single ALD cycle. When the opaque ZrO_2-coated electrodes are immersed in a saturated solution of catechol, electrodes with 0, 1, 2, and 3 ALD cycles of ZrO_2 turn a faint yellow, indicating catechol complexation of residual exposed Ti(IV) sites.[31] ALD growth initiation can be incomplete, giving rise to incomplete surface coverage in subsequent growth cycles.

As can be observed in Figure 2, the number of layers of ZrO_2 deposited on the TiO_2 has a distinct effect on the performance of the solar cells. Solid-state DSC performance parameters, shown in Table 1, are improved only for a few deposition cycles of ZrO_2, boosting power conversion efficiencies from nominal

Surface Passivation of Nanoporous TiO$_2$

J. Phys. Chem. C, Vol. 113, No. 42, 2009 **18387**

TABLE 1: Solid-State DSC Performance Parameters for the Different Deposition Cycles of ZrO$_2$

sample	ZrO$_2$ thickness (Å)	device area (mm^2)	V_{oc} (V)	I_{sc} (mA)	j_{sc} (mA/cm^2)	fill factor	η (%)
0c ZrO$_2$	0	1.6	0.63	0.017	1.1	0.41	0.27
1c ZrO$_2$	1.1	1.1	0.70	0.021	1.9	0.50	0.65
2c ZrO$_2$	2.2	1.0	0.70	0.023	2.3	0.66	1.08
3c ZrO$_2$	3.3	1.1	0.71	0.011	1.0	0.66	0.45

control efficiencies up to a maximum, in the case of two ZrO$_2$ cycles, and then falling back to low efficiencies. Also noteworthy are the unusual shapes of the $j-V$ curves for the samples subjected to zero or one ZrO$_2$ coating cycle.

We note here the relatively low performance of the control device as compared to that reported in previous work,[2,3,22] which can be attributed to variations in fabrication method and the materials used in cell fabrication. Nonetheless, this work clearly shows the distinctive trends achieved in each set of solid-state DSCs by slight modification of the nanoparticle surface composition. While ZrO$_2$ is an insulator, its integration into the electron transporting photoelectrode clearly effects significant improvements in power conversion efficiencies. Below we use IS analysis to probe the origin of these improvements.

Figure 3 shows the impedance spectra obtained for the cells measured under illumination at −0.75 V. The arcs appearing in these figures are attributed to the following effects:

(i) The high-frequency arc shown in Figure 3d is ascribed to spiro-OMeTAD transport resistance together with the effect of interface capacitances at both the gold counter electrode and the TiO$_2$ underlayer.[18,22]

(ii) The low-frequency arc, Figure 3a,b, is attributed to the charge transfer resistance associated with electron recombination at the interface, combined with the chemical capacitance of electrons in the TiO$_2$.[18,19,22]

(iii) Only observed for samples with ZrO$_2$ coatings, a third arc appears at intermediate frequencies, the width of which increases with the number of ZrO$_2$ layers deposited. Therefore, we associate this arc with the presence of the ZrO$_2$ layer.

(iv) Finally, at the lowest frequencies impedance data cross the real axis, indicating the appearance of negative capacitance (or a low-frequency inductance). As can be observed in panels

b−d in Figure 3, this contribution to the impedance is more relevant in the cells with 0 and 1 coating layers of ZrO$_2$ than in the cells with 2 and 3 ZrO$_2$ layers.[23]

Due to the complex interplay between the various contributions to the IS spectra, we restrict our attention to the most relevant parameters, i.e., charge transfer at the TiO$_2$ interface and the chemical capacitance of the TiO$_2$. Thus, the equivalent circuit can be reduced to the combination of a resistance in series to the parallel combination of the low-frequency cell capacitance, C_{cell}, the total recombination resistance of the cell, R_{rec}, and the series association of a resistance and an inductance to account for the negative capacitance contribution.[23] We adopt the notation that forward bias potential is positive, hence the difference between the Fermi level of holes and electrons is related to the bias voltage as

$$V = (E_{Fn} - E_{Fp})/e \qquad (1)$$

where e is the elementary charge, E_{Fn} is the quasi-Fermi level for holes, and E_{Fp} is for electrons.

By using this equivalent circuit a reasonable fit of the impedance spectra can be obtained. Figure 4 shows the resulting values of C_{cell} and R_{rec} as a function of the bias potential. Between 0 and ∼0.15 V, both the values of capacitance and charge transfer resistance are very similar in all the samples. In this region the impedance is dominated by the response of the film back-layer in contact with the spiro-OMeTAD. At potentials higher than ∼0.15 V, the capacitance of the cell is dominated by the chemical capacitance of electrons in nanostructured TiO$_2$ that takes the form[32]

$$C_\mu = C_0 \exp\left[\frac{\alpha}{kT}(E_{Fn} - E_C)\right] = \alpha\frac{e^2}{kT}n_{cb}^\alpha \qquad (2)$$

with E_C the conduction band energy of TiO$_2$, α the factor governing the distribution of trap states below the conduction band, n_{cb} the electron density at conduction band, k the Boltzmann constant, T the temperature, E_{Fn} the Fermi level of electrons in the TiO$_2$, and C_0 a constant. The observation of the exponential behavior of eq 2 indicates that the Fermi level passes through the band gap, and that there is an exponential distribution of traps.[33]

Total recombination resistance is the result of the parallel combination of R_{BL}, the resistance accounting for losses at the TiO$_2$ compact layer uncoated by the nanoporous matrix (the back layer), and R_r, the recombination from the TiO$_2$ film, thus $R_{rec} = R_{BL} \| R_r$. At potentials higher than ∼0.15 V, R_r dominates and, as a general rule, the charge transfer losses from TiO$_2$ may be described with a recombination (interception) resistance that follows,[21,34]

$$R_r = R_0 \exp\left[\frac{\beta}{kT}(E_{Fn} - E_{Fp})\right] \qquad (3)$$

with β the transfer coefficient, E_{Fp} the Fermi level of holes in
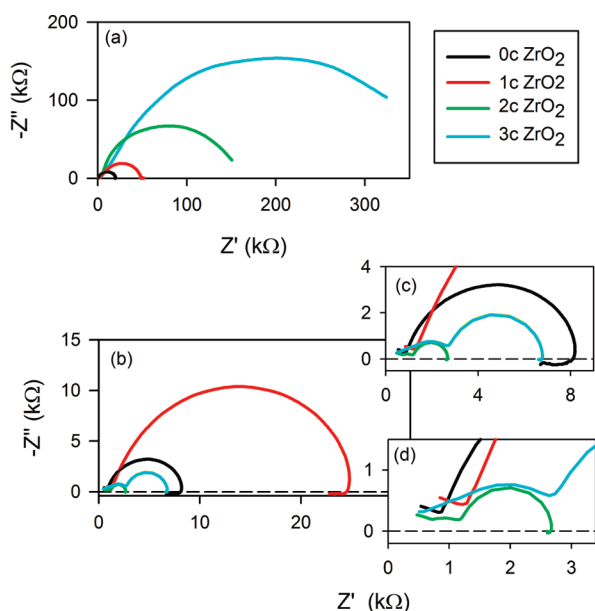

Figure 3. Impedance spectra of solid-state DSC at 0.4 (a) and 0.75 V (b−d) forward bias with increasing number of cycles of ZrO$_2$ deposition. Panels c and d are magnifications of panel b.
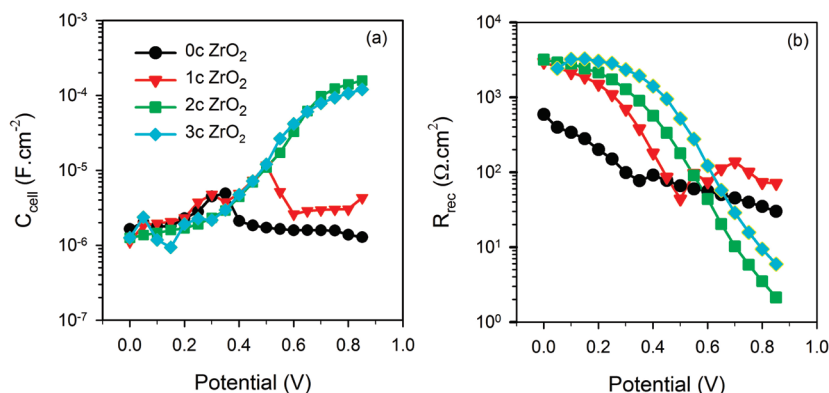
Figure 4. (a) Capacitance and (b) recombination resistance of solid-state DSCs with increasing number of cycles of ZrO_2 deposition under 100 mW/cm^2 illumination.

the spiro-OMeTAD, and R_0 a parameter that depends on the temperature and the characteristics of the recombining interface. The parameter β is often associated with classical Butler–Volmer behavior; however, in DSCs this parameter has been interpreted in terms of recombination through surface states.[21]

As can be seen in Figure 4, only samples coated with two or more ZrO_2 layers follow the behavior described by eqs 2 and 3. The decrease in the slope at the highest potentials in both C_μ and R_r is due to the potential drop at the series resistance of the cell. This series resistance is associated with transport in the charge transport medium, FTO glass, and eventually hole regeneration at the counterelectrode.[34]

In contrast to the above results, the uncoated sample and the one with a single ZrO_2 coating cycle show a very different response: The capacitance exhibits a peak, while at the same potential the recombination resistance shows a minimum (Figure 4). This behavior of C_{cell} and R_{rec} has been previously attributed to the presence of a localized energy trap state at the TiO_2 surface.[35] Beyond this peak, the capacitance tends to a low, constant value instead of following the exponential rise described by eq 2, as was also observed in other low-efficiency cells.[23] At the same time, a large low-frequency inductive (or negative capacitance) effect is evident for samples with zero and one coating cycle, panels b and c in Figure 3. The high photopotential obtained, even at these low coating levels, suggests that the Fermi level is being raised inside the TiO_2, increasing n_{cb}. Therefore, we attribute the low value found for the capacitance to the effect of the low-frequency inductance observed in the impedance.

Inductive behavior at low frequency is frequently found in nanocomposite-based solar cells.[23] So far, a definitive interpretation of this effect has not been provided. However, the inductive behavior can be generally related to a charge transfer process between two electronic reservoirs that is governed by the occupation of an intermediate state, which becomes saturated and limits the kinetics of the process.[36] The presence of this inductive behavior is a limiting factor for photovoltaic conversion and normally is an indicator of low solar cell performance.[23]

From the experimental evidence in Figures 3 and 4, we propose that in the present system, the initial and final states for the electrons are the TiO_2 conduction band and the spiro-OMeTAD HOMO, respectively. The charge transfer associated with recombination is mediated by the surface states at the interface between the electron and hole conductors, limiting the cell performance in the samples with zero and one layer of ZrO_2. As many of these surface states are suppressed by the additional coating layers, the inductance effect also decreases, allowing the emergence of the standard chemical capacitance C_μ that
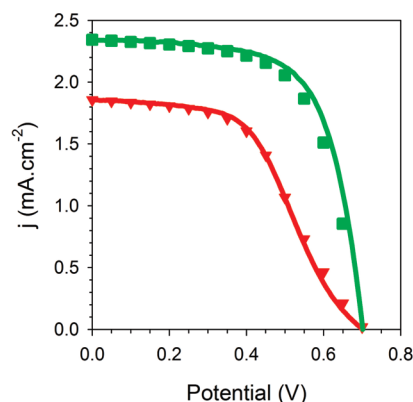

Figure 5. Solid-state DSC j–V curves at 100 mW/cm^2 illumination (lines) and j–V curve generated from impedance data (dots) with increasing numbers of ZrO_2 deposition cycles: one ZrO_2 layer (red line and ▼); two ZrO_2 layers (green line and ■). The difference in shape is given by the differences in R_{rec}.

behaves as described previously for conventional liquid electrolytes and high-efficiency solid-state DSCs.[21,22,33]

Focusing attention now on R_{rec} in Figure 4, we can observe that for potentials below 0.4 V, the recombination resistance progressively increases with increasing thickness of the ZrO_2 barrier material; see also the impedance in Figure 3a. This shows that inserting a physical barrier improves the collection efficiency by diminishing recombination losses between the TiO_2 and spiro-OMeTAD. In particular, a remarkable improvement is observed in the back-layer recombination resistance after the first layer of ZrO_2 is deposited. This is presumably the origin of the lower current density observed for the uncoated sample. In contrast, for the sample treated with three cycles of ZrO_2, although V_{oc} increases further, j_{sc} decreases, resulting in the smaller overall efficiency obtained with respect to the 2-layer device. The data from Figure 5 indicate that the conduction bands in samples 2 and 3 are at the same position, and that the dye absorbed by the films is the same. Therefore, we may attribute this decrease in j_{sc} to excessive ZrO_2 coverage, which inhibits electron injection by the photoexcited dye into the TiO_2.

Impedance data can be used to describe the influence of the internal resistances of the cell on the j–V curve. Provided that j_{sc} is known, the full j–V curve can be calculated through[34]

$$j = j_{sc} - \frac{1}{S} \int_0^V \frac{dV}{R_{total}} \tag{4}$$

where S is the cell surface and R_{total} is the sum of R_{rec} and the

Surface Passivation of Nanoporous TiO$_2$

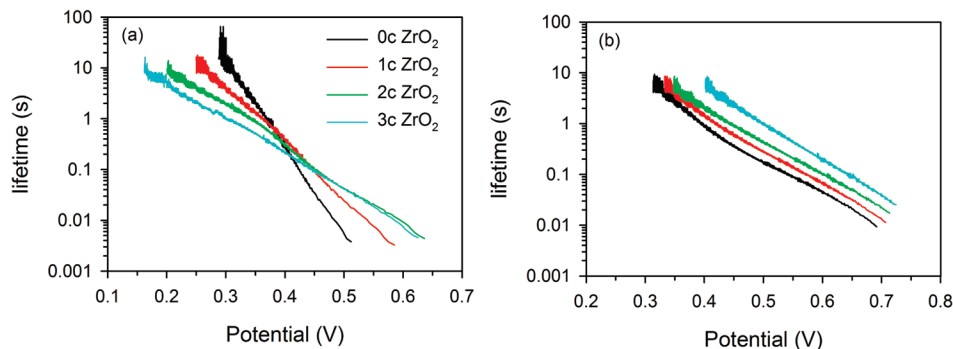*J. Phys. Chem. C, Vol. 113, No. 42, 2009* **18389**

Figure 6. Charge lifetimes from open-circuit photovoltage decay measurements of DSCs with increasing numbers of cycles of ZrO$_2$ deposition for both (a) spiro-OMeTAD and (b) liquid electrolyte as hole conductors.

total series resistance arising from the FTO, spiro-OMeTAD, counter electrode, etc. Even with the simple equivalent circuit proposed to describe the IS data, good agreement is found between the results from the impedance spectroscopy and the original $j-V$ curve under illumination, as shown in Figure 5. For simplicity, only samples with one and two ZrO$_2$ layers are represented in this plot.

As can be observed in Figure 3, the primary contribution to the total resistance of the cell is R_{rec} in all cases. This is therefore the principal element determining the shape of the $j-V$ curve and thus the steady-state DC characteristics of the solar cell. In fact, for the sample with one ZrO$_2$ layer, we observe that the valley at 0.5 V is responsible for the $j-V$ curve bend at this potential, reducing the fill factor 24% with respect to the 66% obtained for the two-layer ZrO$_2$ coated sample. The same effect is even more prominent for the uncoated sample, reflecting the lowering of the β value, and therefore yielding a smaller $R_{rec}-V$ slope (Figure 4b).[34] In contrast, the cells with two and three ZrO$_2$ layers exhibit higher $R_{rec}-V$ slopes, providing the largest FFs found in this device series (Table 1). Therefore, we can conclude that the addition of extra ZrO$_2$ layers suppresses most of these surface states, yielding acceptable shapes for the C_{cell}, R_{rec}, and $j-V$ plots.

An alternative technique to study the interception of injected electrons by spiro-OMeTAD is open-circuit photovoltage decay.[37] In this measurement, the cell first is allowed to achieve a stationary state under 1 sun illumination, then the lamp is turned off to observe the open-circuit voltage, V_{oc}, decay in complete darkness. Assuming that recombination in the dark occurs only within the hole-transporting medium, the rate of the decay can be directly related to the electron lifetime, as shown by eq 5.

$$\tau_n = -\frac{kT}{e}\left(\frac{dV_{oc}}{dt}\right)^{-1} \tag{5}$$

The charge lifetimes determined from the open-circuit voltage decay measurements are shown in Figure 6. From the ssDSC open-circuit decay plots, increases in charge lifetime are observed at high photovoltages. However, a slower decay response is seen at lower photovoltages. It is possible to describe these responses in terms of the results obtained from impedance. The electron lifetime is obtained from IS data via the expression

$$\tau_n = R_r C_\mu \tag{6}$$

For samples with zero and one ZrO$_2$ layer, the capacitance is nearly constant, and thus the lifetime slope is dominated by the

transfer factor of R_r, i.e., $\tau_n \propto \exp\left[-\beta\, eV/kT\right]$. However, in the cases of two and three ZrO$_2$ layers, the capacitance varies exponentially (eq 2) and thus the slope of τ_n is dominated by the difference between the transfer and tail distribution factors: $\tau_n \propto \exp\left[(\alpha - \beta)\, eV/kT\right]$, yielding a lower slope for the $\tau-V$ plot. Note that V_{oc}-decay is a dark measurement while data from impedance are taken under illumination. However, the differences in these measurement conditions affect R_r but not C_μ.

As a comparison, liquid-electrolyte DSCs modified with ALD-ZrO$_2$ layers in the same manner were also characterized by V_{oc}-decay. Charge lifetimes are successively shifted to larger values with increasing cycles of ZrO$_2$ on the nanoparticulate TiO$_2$ electrode. In these cells we expect that the chemical capacitance is only slightly affected by the number of layers of ZrO$_2$ while the recombination resistance is expected to exhibit higher values with increasing numbers of ZrO$_2$ layers. In fact, no changes are observed between $\tau-V$ slopes of liquid and solid state DSCs with two and three ZrO$_2$ layers.

Conclusions

The performance of solid-state DSCs exhibits substantial enhancement following photoelectrode coating with ZrO$_2$ by atomic layer deposition. Current densities increase for up to two cycles of zirconium dioxide deposited on the photoelectrode. However, for thicker ZrO$_2$ coatings, the photocurrent decreases due to difficulties in charge injection from the dye to the semiconductor. From impedance spectroscopy we find that the ZrO$_2$ coating produces a barrier between electron and hole transport media, decreasing recombination (interception) and suppressing the activity of surface recombination sites. As a consequence, increases in both current densities and FFs of the ssDSCs are observed. We also find that charge transfer via surface states can account for the existence of an inductive effect at low frequencies that limits the performance of the solar cells.

References and Notes

(1) Grätzel, M. *Inorg. Chem.* **2005**, *44*, 6841.
(2) (a) Bach, U.; Lupo, D.; Comte, P.; Moser, J. E.; Weissörtel, F.; Salbeck, J.; Spreitzer, H.; Grätzel, M. *Nature* **1998**, *395*, 583. (b) Snaith,

18390 *J. Phys. Chem. C, Vol. 113, No. 42, 2009*

Li et al.

H. J.; Karthikeyan, C. S.; Petrozza, A.; Teuscher, J.; Moser, J. E.; Nazeeruddin, M. K.; Thelakkat, M.; Grätzel, M. *J. Phys. Chem. C* **2008**, *112*, 7562.

(3) Jennings, J. R.; Peter, L. M. *J. Phys. Chem. C* **2007**, *111*, 16100.

(4) Martinson, A. B. F.; Hamann, T. W.; Pellin, M. J.; Hupp, J. T. *Chem.—Eur. J.* **2008**, *14*, 4458.

(5) Snaith, H. J.; Schmidt-Mende, L. *Adv. Mater.* **2007**, *19*, 3187.

(6) Hamann, T. W.; Jensen, R. A.; Martinson, A. B. F.; Ryswyk, H. V.; Hupp, J. T. *Energy Environ. Sci.* **2008**, *1*, 66.

(7) Bisquert, J. *J. Phys. Chem. C* **2007**, *111*, 17163.

(8) Handa, S.; Wietasch, H.; Thelakkat, M.; Durrant, J. R.; Haque, S. A. *Chem. Commun.* **2007**, 1725.

(9) Snaith, H. J.; Grätzel, M. *Appl. Phys. Lett.* **2006**, *89*, 262114.

(10) Schmidt-Mende, L.; Zakeeruddin, S. M.; Grätzel, M. *Appl. Phys. Lett.* **2005**, *86*, 013504.

(11) (a) Fabregat-Santiago, F.; Garcia-Canadas, J.; Palomares, E.; Clifford, J. N.; Haque, S. A.; Durrant, J. R.; Garcia-Belmonte, G.; Bisquert, J. *J. Appl. Phys.* **2004**, *96*, 6903. (b) Handa, S.; Haque, S. A.; Durrant, J. R. *Adv. Funct. Mater.* **2007**, *17*, 2878.

(12) Zhang, X. T.; Sutanto, I.; Taguchi, T.; Meng, Q. B.; Rao, T. N.; Fujishima, A.; Watanabe, H.; Nakamori, T.; Uragami, M. *Sol. Energy Mater. Sol. Cells* **2003**, *80*, 315.

(13) Taguchi, T.; Zhang, X. T.; Sutanto, I.; Tokuhiro, K.; Rao, T. N.; Watanabe, H.; Nakamori, T.; Uragami, M.; Fujishima, A. *Chem. Commun.* **2003**, 2480.

(14) Kay, A.; Grätzel, M. *Chem. Mater.* **2002**, *14*, 2930.

(15) Puurunen, R. L. *J. Appl. Phys.* **2005**, *97*, 121301.

(16) (a) Hamann, T. W.; Farha, O. K.; Hupp, J. T. *J. Phys. Chem. C* **2008**, *112*, 19756. (b) Martinson, A. B. F.; Elam, J. W.; Liu, J.; Hupp, J. T.; Pellin, M. J.; Marks, T. J. *Nano Lett.* **2008**, *8*, 2862. (c) Standridge, S.; Schatz, G. C.; Hupp, J. T. *J. Am. Chem. Soc.* **2008**, *130*, 8598. (d) Hamann, T. W.; Martinson, A. B. F.; Elam, J. W.; Pellin, M. J.; Hupp, J. T. *Adv. Mater.* **2008**, *20*, 1560. (e) Hamann, T. W.; Martinson, A. B. F.; Elam, J. W.; Pellin, M. J.; Hupp, J. T. *J. Phys. Chem. C* **2008**, *112*, 10303. (f) Martinson, A. B. F.; Elam, J. W.; Hupp, J. T.; Pellin, M. J. *Nano Lett.* **2007**, *7*, 2183.

(17) Law, M.; Greene, L. E.; Radenovic, A.; Kuykendall, T.; Liphardt, J.; Yang, P. *J. Phys. Chem. B* **2006**, *110*, 22652.

(18) Fabregat-Santiago, F.; Bisquert, J.; Palomares, E.; Haque, S. A.; Durrant, J. R. *J. Appl. Phys.* **2006**, *100*, 034510.

(19) Fabregat-Santiago, F.; Bisquert, J.; Garcia-Belmonte, G.; Boschloo, G.; Hagfeldt, A. *Sol. Energy Mater. Sol. Cells* **2005**, *87*, 117.

(20) Bisquert, J. *J. Phys. Chem. B* **2002**, *106*, 325.

(21) Wang, Q.; Ito, S.; Grätzel, M.; Fabregat-Santiago, F.; Mora-Seró, I.; Bisquert, J.; Bessho, T.; Imai, H. *J. Phys. Chem. B* **2006**, *110*, 25210.

(22) Fabregat-Santiago, F.; Bisquert, J.; Cevey, L.; Chen, P.; Wang, M.; Zakeeruddin, S. M.; Grätzel, M. *J. Am. Chem. Soc.* **2009**, *131*, 558.

(23) Mora-Seró, I.; Bisquert, J.; Fabregat-Santiago, F.; Garcia-Belmonte, G.; Zoppi, G.; Durose, K.; Proskuryakov, Y.; Oja, I.; Belaidi, A.; Dittrich, T.; Tena-Zaera, R.; Katty, A.; Lévy-Clement, C.; Barrioz, V.; Irvine, S. J. C. *Nano Lett.* **2006**, *6*, 640.

(24) Pingree, L. S. C.; Russell, M. T.; Marks, T. J.; Hersam, M. C. *J. Appl. Phys.* **2006**, *100*, 044502-1-10.

(25) Pangborn, A. B.; Giradello, M. A.; Grubbs, R. H.; Rosen, R. K.; Timmers, F. J. *Organometallics* **1996**, *15*, 1518.

(26) Chun, C. M.; Kim, M. J.; Vak, D.; Kim, D. Y. *J. Mater. Chem.* **2003**, *13*, 2904.

(27) Schmidt-Mende, L.; Kroeze, J. E.; Durrant, J. R.; Nazeeruddin, M. K.; Grätzel, M. *Nano Lett.* **2005**, *5*, 1315.

(28) Kavan, L.; Grätzel, M. *Electrochim. Acta* **1995**, *40*, 643.

(29) Krüger, J.; Plass, R.; Cevey, L.; Piccirelli, M.; Grätzel, M.; Bach, U. *Appl. Phys. Lett.* **2001**, *79*, 2085.

(30) Ito, S.; Nazeeruddin, M. K.; Liska, P.; Comte, P.; Charvet, R.; Pechy, P.; Jirousek, M.; Kay, A.; Zakeeruddin, S. M.; Grätzel, M. *Prog. Photovoltaics* **2006**, *14*, 589.

(31) Guo, J.; She, C.; Lian, T. *J. Phys. Chem. C* **2007**, *111*, 8979.

(32) (a) Fabregat-Santiago, F.; Mora-Seró, I.; Garcia-Belmonte, G.; Bisquert, J. *J. Phys. Chem. B* **2003**, *107*, 758. (b) Bisquert, J. *Phys. Chem. Chem. Phys.* **2003**, *5*, 5360.

(33) Bisquert, J.; Fabregat-Santiago, F.; Mora-Seró, I.; Garcia-Belmonte, G.; Barea, E. M.; Palomares, E. *Inorg. Chim. Acta* **2008**, *361*, 684.

(34) Fabregat-Santiago, F.; Bisquert, J.; Palomares, E.; Otero, L.; Kuang, D.; Zakeeruddin, S. M.; Grätzel, M. *J. Phys. Chem. C* **2007**, *111*, 6550.

(35) Mora-Seró, I.; Bisquert, J. *Nano Lett.* **2003**, *3*, 945.

(36) Bisquert, J.; Garcia-Belmonte, G.; Montero, J. M.; Bolink, H. J. *Proc. SPIE Int. Soc. Opt. Eng.* **2006**, *6192*, 619210.

(37) (a) Zaban, A.; Greenshtein, M.; Bisquert, J. *ChemPhysChem* **2003**, *4*, 859. (b) Bisquert, J.; Zaban, A.; Greenshtein, M.; Mora-Seró, I. *J. Am. Chem. Soc.* **2004**, *126*, 13550.

JP906573W